Disaster Resilient and Self-Assessing Multifunctional Transportation Structures

Project No. 18STTAM02

Lead University: Texas A&M University

TECHNICAL DOCUMENTATION PAGE

1. Project No. 18STTAM02	2. Government Accession No.	3. Recipient's Catalog No.		
4. Title and Subtitle Disaster-Resilient and Self-Assessing Multifunctional Transportation Structures		**5. Report Date** Aug. 2019		
		6. Performing Organization Code		
7. Author(s) PI: Ibrahim Karaman https://orcid.org/0000-0001-6461-4958 Co-PI: Darren Hartl https://orcid.org/0000-0001-9922-0481		**8. Performing Organization Report No.**		
9. Performing Organization Name and Address Transportation Consortium of South-Central States (Tran-SET) University Transportation Center for Region 6 3319 Patrick F. Taylor Hall, Louisiana State University, Baton Rouge, LA 70803		**10. Work Unit No. (TRAIS)**		
		11. Contract or Grant No. 69A3551747106		
12. Sponsoring Agency Name and Address United States of America Department of Transportation Research and Innovative Technology Administration		**13. Type of Report and Period Covered** Final Research Report Mar. 2018 – Mar. 2019		
		14. Sponsoring Agency Code		
15. Supplementary Notes Report uploaded and accessible at Tran-SET's website (http://transet.lsu.edu/).				

16. Abstract

This research designs and characterizes multifunctional materials, in particular inexpensive shape memory alloys, for transportation structures that possess excellent mechanical properties and self-sensing capabilities for strengthening and health monitoring. The properties are the Fe-SMAs are sensitive to part size in that the grain size of the material, which can be grown to several inches, should exceed the smallest dimension of the part. In the current work, maximum part size of the large dimension Fe-SMA rods were determined through detailed microstructural investigations. Samples were subjected to abnormal grain growth heat treatments and found out that part size be increased up to 4.6 mm. Work to correlate computational and experimental work concerning the magnetic sensing of Fe-SMA transformation was conducted using via tensile loading of Fe-SMA wire. A model was developed to simulate a grain by grain transformation of a wire with large (4mm) grains along the wire, modeled as partitioned segments.

17. Key Words Shape memory alloys, Fe-SMA rod, structural optimization, health monitoring, multifunctional materials, magnetic sensing		**18. Distribution Statement** No restrictions. This document is available through the National Technical Information Service, Springfield, VA 22161.		
19. Security Classif. (of this report) Unclassified	**20. Security Classif. (of this page)** Unclassified		**21. No. of Pages** 28	**22. Price**

Form DOT F 1700.7 (8-72)   **Reproduction of completed page authorized.**

SI* (MODERN METRIC) CONVERSION FACTORS

APPROXIMATE CONVERSIONS TO SI UNITS

Symbol	When You Know	Multiply By	To Find	Symbol
LENGTH				
in	inches	25.4	millimeters	mm
ft	feet	0.305	meters	m
yd	yards	0.914	meters	m
mi	miles	1.61	kilometers	km
AREA				
in^2	square inches	645.2	square millimeters	mm^2
ft^2	square feet	0.093	square meters	m^2
yd^2	square yard	0.836	square meters	m^2
ac	acres	0.405	hectares	ha
mi^2	square miles	2.59	square kilometers	km^2
VOLUME				
fl oz	fluid ounces	29.57	milliliters	mL
gal	gallons	3.785	liters	L
ft^3	cubic feet	0.028	cubic meters	m^3
yd^3	cubic yards	0.765	cubic meters	m^3
NOTE: volumes greater than 1000 L shall be shown in m^3				
MASS				
oz	ounces	28.35	grams	g
lb	pounds	0.454	kilograms	kg
T	short tons (2000 lb)	0.907	megagrams (or "metric ton")	Mg (or "t")
TEMPERATURE (exact degrees)				
^oF	Fahrenheit	5 (F-32)/9 or (F-32)/1.8	Celsius	^oC
ILLUMINATION				
fc	foot-candles	10.76	lux	lx
fl	foot-Lamberts	3.426	candela/m^2	cd/m^2
FORCE and PRESSURE or STRESS				
lbf	poundforce	4.45	newtons	N
lbf/in^2	poundforce per square inch	6.89	kilopascals	kPa

APPROXIMATE CONVERSIONS FROM SI UNITS

Symbol	When You Know	Multiply By	To Find	Symbol
LENGTH				
mm	millimeters	0.039	inches	in
m	meters	3.28	feet	ft
m	meters	1.09	yards	yd
km	kilometers	0.621	miles	mi
AREA				
mm^2	square millimeters	0.0016	square inches	in^2
m^2	square meters	10.764	square feet	ft^2
m^2	square meters	1.195	square yards	yd^2
ha	hectares	2.47	acres	ac
km^2	square kilometers	0.386	square miles	mi^2
VOLUME				
mL	milliliters	0.034	fluid ounces	fl oz
L	liters	0.264	gallons	gal
m^3	cubic meters	35.314	cubic feet	ft^3
m^3	cubic meters	1.307	cubic yards	yd^3
MASS				
g	grams	0.035	ounces	oz
kg	kilograms	2.202	pounds	lb
Mg (or "t")	megagrams (or "metric ton")	1.103	short tons (2000 lb)	T
TEMPERATURE (exact degrees)				
^oC	Celsius	1.8C+32	Fahrenheit	^oF
ILLUMINATION				
lx	lux	0.0929	foot-candles	fc
cd/m^2	candela/m^2	0.2919	foot-Lamberts	fl
FORCE and PRESSURE or STRESS				
N	newtons	0.225	poundforce	lbf
kPa	kilopascals	0.145	poundforce per square inch	lbf/in^2

TABLE OF CONTENTS

LIST OF FIGURES

ACRONYMS, ABBREVIATIONS, AND SYMBOLS

FEA   Finite Element Analysis

GMR   Giant Magneto-Resistive

MSMA   Magnetic Shape Memory Alloy

SHM   Structural Health Monitoring

SMA   Shape Memory Alloy

XFEM   Extended Finite Element Method

EXECUTIVE SUMMARY

Shape memory alloy (SMAs) can produce large recoverable deformations triggered by stress in a response known as superelasticity. This response has been shown to limit the damage sustained by the structure from adverse event such as earthquakes and have been considered in a range of civil engineering applications. The most widespread SMA candidate for such applications is the NiTi SMA, which is cost-prohibitive for large scale applications. Instead, a low-cost and easily processed iron-based SMA is provides a more suitable alternative in structural applications. Furthermore, the Fe-SMA shows an interesting meta-magnetic shape memory response, where a change in induced magnetization of the material occurs from applied stress and can be easily detected using commercial magnetometers. This property can be harnessed to create a method to monitor the stresses and strains on structural systems with Fe-SMAs remotely and in a non-destructive fashion. The combination of these properties enables a new kind of structural health monitoring framework where the load-bearing and sensing elements are the same and quantitative information could be collected in real-time with simple instruments.

The goal of the project is to create large dimension Fe-SMA rods and that are suitable for structural and transportation applications and determine the maximum part size. To accomplish this 2mm and 4.6 mm dimeter Fe-SMA rods were fabricated through extrusion. Abnormal grain growth heat treatments were performed, and detailed microstructural characterizations were performed using optical microscopy and electron backscatter diffraction techniques (EBSD). Abnormal grain growth heat treatments results in large bamboo like morphology which is important for obtaining an excellent superelastic response for Fe-SMAs. Experimental results showed that maximum part size for Fe-SMAs can be increased up to 4.6 mm using abnormal grain growth heat treatments. Bulk-Fe-SMA rods and cables that are capable of sustaining high stress and elongation. Optimal configuration of rods and sensors were computationally determined through combined magnetic-mechanical modeling and validated through experiments.

This work leverages past successes in the analysis and design of shape memory components to consider for the first time the magneto-mechanical response of 1-D and 2-D architectures formed from Fe-SMA wires and rods as embedded in structural matrix appropriate for transportation infrastructure. Through a combined approach of physics-based modeling, optimization and materials design, this research achieves advantageous mechanical properties and self-monitoring capabilities in a single material for transportation structures. The developed multifunctional composites are expected transform the design, construction, and rehabilitation of infrastructure systems. Additionally, the project will define a viable path for technology transfer by establishing substantive partnerships with commercial alloy manufacturers and cultivate the awareness.

1. INTRODUCTION

Common seismic detection in transportation structures include reinforced concreate design that are capable of dissipating energy through inelastic deformation. Although these design concepts improve the ductility of the structure, they usually suffer from concrete cracking or support beam separation due to displacement incompatibility between seismic frame and the structure. One of the main drawbacks of this design strategy is significant post-event damage. This problem poses a great challenge to transportation infrastructures after natural disasters such as earthquakes or hurricanes, since undetected damages after these events increases the uncertainty of the structure. As a result, potential public treat becomes much more serious in these structures than visibly damaged ones. Moreover, damage assessment of bridges, roadways and other transportation structures can be very time-consuming and delay their reoperation. Therefore, there is a need for next generation structures with innovative strategies to assess the structural integrity and detect hidden damages after natural disasters. One of the potential solutions to overcome this problem is integrating multifunctional materials to transportation structures. Smart materials can provide simultaneous sensing capabilities with simplified designs, reduced material use and less manufacturing complexity.

Shape memory materials (SMA) with superelastic properties can recover large deformations triggered by change in stress. Since the loading and unloading paths do not coincide, a hysteresis loop occurs, which signifies energy dissipation. Due to these unique properties, superelastic SMAs materials have been considered in wide range of civil engineering applications, such as bracing systems *(1, 2)* connectors *(3)*, and concreate reinforcement *(4-6)*. As a result, the damage sustained by the structure from adverse events have been decreased and crack propagation has been prevented. Current candidate for such applications is a very well-known NiTi-based alloy called 'Nitinol'. However, NiTi alloys are expensive, are difficult to process and weld at large scales, have a limited range of operating temperatures and limited fatigue resistance *(7-9)*. Also, since NiTi SMAs have mainly been used in medical applications, there is an overall lack of supply in SMAs in large sizes and volumes. The recent discovery of inexpensive Fe-SMAs *(10-15)* that have superelasticity and energy dissipation similar to NiTi but with good workability and a cost/weldability on par with advanced high strength steels. Additionally, Fe-SMAs possess interesting meta-magnetic response where significant change in magnetic properties occur during superelasticity. This property can be used to remotely detect internal stresses in the infrastructure and convert them into measurable signal using commercial magnetometers. A new kind of structural health monitoring framework can be integrated into current infrastructures that allows continuous assessment of structural integrity throughout the life of the part.

However, adoption of the technology is slowed by two technical barriers. First, the size of useful parts in transportation structures is often large and the geometry diverse. The properties are the Fe-SMAs are sensitive to part size in that the grain size of the material, which can be grown to several inches, should exceed the smallest dimension of the part. However, the maximum grain size, and thus maximum possible dimension of the part is currently unknown. Second, the information resolution and accuracy of the magnetic sensing property is not yet known, and the optimal configuration of sensor and structural components has not been determined. This project aims to overcome both barrier through a combined experiment-modeling validation approach to simultaneously achieve advantageous mechanical properties and structural health monitoring capabilities in a single multifunctional material. The developed multifunctional technology will enable damage detection, limit progressive damage, extend service life and provide re-centering

capabilities. As a result, structural performance, durability, sustainability, and resiliency of the structure will be increased. Furthermore, the project will cultivate the awareness and expertise in the technology through workforce development and outreach activities and will define a viable path for technology transfer by establishing substantive partnerships with commercial alloy manufacturers.

2. OBJECTIVES

The objective of this research is to design and characterize multifunctional materials, in particular inexpensive shape memory alloys, for transportation structures that possess excellent mechanical properties and self-sensing capabilities for strengthening and health monitoring. The system exploits unique properties of recently developed low-cost superelastic FeMnAlNi shape memory alloys (SMAs), which shows temperature invariant superelastic properties, high strength and self-sensing in structural health monitoring. In this project, large dimension Fe-SMA rods and that are suitable for structural and transportation applications are created and maximum part size is determined. It will be demonstrated that bulk Fe-SMA rods and cables that are capable of sustaining high stress and elongation. Optimal configuration of rods and sensors are computationally determined through combined magnetic-mechanical modeling and validated through experiments. For the implementation phase of the project, we will show that the strain in large size Fe-SMA directly correlates with changes in its magnetic response. The research addresses the following research tasks:

Design, fabrication and characterization (Technical):
- Design topology and configuration of bulk Fe-SMA rods and cables in cementitious composites for optimal magnetic sensing capabilities.
- Determine maximum Fe-SMA component size through microstructural characterization and validation experiments.

Demonstration of structural health monitoring capability (Implementation):
- Demonstration of self-assessing capabilities in a realistic infrastructure system.

3. LITERATURE REVIEW

3.1. Fe-based Shape Memory Alloys

With increasing demand for better infrastructural performance, "smart materials" have received considerable attention. A particularly appealing and interesting class of smart materials is shape memory alloys (SMAs), which can "remember" their original shape upon being deformed as a result of solid-to-solid phase transformations. Superelastic SMAs can recover large deformations (up to 7–8% strain) upon unloading without the help of any external stimuli. Due to their excellent passive re-centering and good energy absorbing capabilities, the superelastic SMAs have been considered in a wide range of applications in civil engineering and structural applications *(2, 16-24)*. Commercially available SMAs such as nickel-titanium (NiTi) alloys show excellent superelastic properties, but they are expensive, difficult to process and weld at large scales, and have limited range of operating temperatures and limited fatigue resistance *(7-9)*. Recently, inexpensive FeMnAlNi SMA have been developed showing large full-recoverable superelasticity at room temperature and high strength (exceeding 1 GPa). Specifically, the recent introduction of a magnetic Fe43.5Mn34Al15Ni7.5 (FMAN) SMA *(12-14, 25)* has provided solution to the poor load-bearing capabilities in magnetic shape memory alloys (MSMAs). This material demonstrates a combination of meta-magnetic shape memory effect and robust mechanical properties suitable for structural applications.

The PI has successfully produced the material in polycrystalline form and demonstrated tensile strength over 800 MPa and ductility exceeding 10% strain, making it one of the first MSMAs capable of exhibiting simultaneous self-sensing and self-centering when applied in an infrastructure system *(12)*. The FeMnAlNi SMA, in particular, also shows an intriguingly wide temperature range from -196°C to 240°C where superelasticity can be observed, compared to an approximate range between -20°C and 80°C in conventional NiTi SMAs *(10)*. This is crucial, especially in infrastructures in regions with extreme climates, which require a stable superelastic response over a broad temperature range. In other words, capabilities of the material will remain unaffected by the ambient temperature, and the technology can be used without modifications in both very hot and very cold climates. The PI has performed systematic studies on the processing and physical metallurgy aspects of the $Fe_{43.5}Mn_{34}Al_{15}Ni_{7.5}$ SMA and have published a number of papers on these topics *(11, 13-15, 25-28)*. Through a combination of precipitation hardening and grain size control techniques developed by the PI *(15, 28)*. We have demonstrated high-strength FMAN polycrystalline wires showing large and fully reversible superelastic strains near 7%.
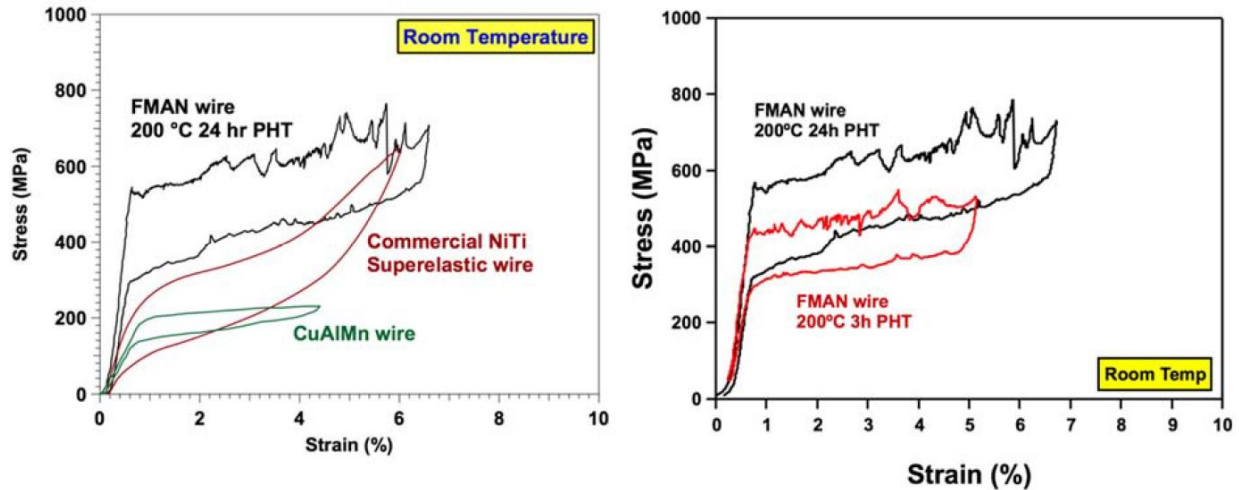
Figure 1. Comparison of the superelastic response of a FMAN wire with wires made of a conventional NiTi *(31)* **and CuAlMn** *(32)* **alloys.**

Figure 1 shows the stress-strain response of a FMAN wire with 24 hour precipitation heat treatment at 200 °C. Compared to a conventionally processed nickel-rich NiTi superelastic alloy, the FMAN SMA shows a similar strength level and comparable level of transformation strain and energy dissipation (stress hysteresis) while exhibiting somewhat higher initial stiffness. On the other hand, both FMAN and NiTi are significantly stronger than CuAlMn SMAs, and possess the ability to dissipate larger amount of energy per cycle. It is worth noting that the transformation stress level of the FMAN SMA can be easily increased or decreased by changing duration of the precipitation heat treatment at 200 °C. For example, the 24-hour heat-treated case shown in Figure 1 produces a high transformation stress of 520 MPa. However, a lower transformation level may be desired in order to allow the self-centering response to trigger at lower deformation levels, for example where a transformation stress level of 400 MPa is obtained when the heat treatment at 200 °C is shortened to 3 hours.

To achieve reversible superelasticity, grain size of an FMAN alloy should be comparable to or larger than the smallest sample dimension. The PI has reported the techniques necessary for controlling the grain size of the material as shown in Figure 2; here, a number of heating/cooling cycles from 1200 °C to room temperature are repeated before the precipitation heat treatment, and the grain size obtained increases monotonically with the number of cycles *(29)*. With this heat 4 treatment, grain sizes larger than 7 mm can be achieved. Figure 2 shows the grain size in wires/rods with various diameters after five heat treatment cycles. In any case, a bamboo-like grain structure is observed when the cross section of the wire contains only one grain, where the wire is a series of single crystals akin to a string of pearls and the grain boundary is minimized. The bamboo-like grain morphology, or *oligocrystalinity*, is important for obtaining an excellent superelastic response for the FMAN material.

5
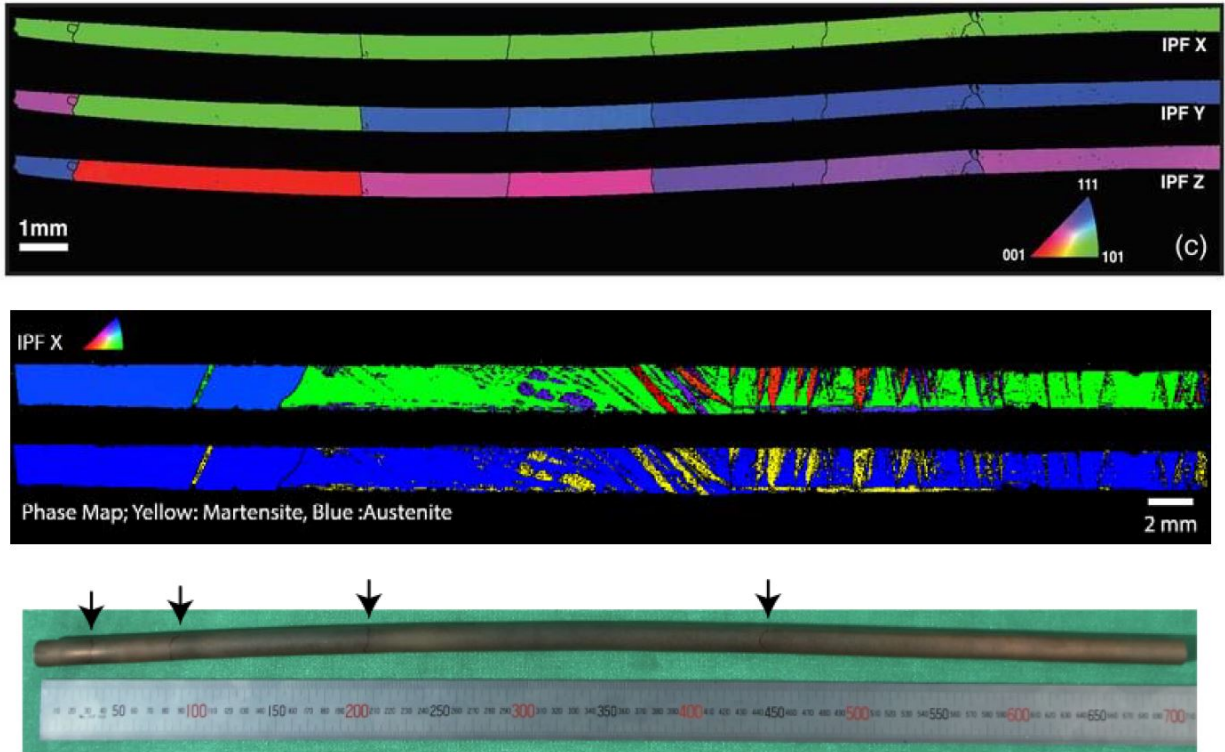
Figure 2. Electron back-scatter diffraction (EBSD) map of FMAN samples of 0.5-mm-diameter wire (top) and 2-mm-diameter wire (center), where a grain size exceeding 10 mm can be found; the same technique has been shown in a CuAlMn alloy (bottom) to obtain a grain size exceeding 200 mm *(33)*.

3.2. Magnetic Structural Sensing

Recently, Magnetic SMAs (MSMAs) have emerged as an interesting extension to SMAs due to their capability of coupling magnetic and electrical energy to thermal and mechanical energy and vice versa. MSMAs allow magnetic field to be used in place of temperature or stress, generating a wide range of new possibilities such as magnetic-field induced shape change, power generation through mechanical deformation, and magnetic heating or cooling due to giant magnetocaloric effect *(30-39)*. There are two possible mechanisms for obtaining the above functionalities in MSMAs. The first involves the field and stress-induced reorientation of martensite variants. If the magnetocrystalline anisotropy energy (MAE) of a magnetic field-favored martensite variant is larger than the energy required for twin boundary motion, that variant will grow at the expense of others, resulting in a magnetic field-induced strain (MFIS). However, the robustness of the mechanism is limited by low actuation stress levels of usually less than 5 MPa *(32-34,38-41)*, which precludes the material from any type of load-bearing applications. In addition, the properties are highly dependent on crystallographic orientation. Thus, the mechanism is limited only to single crystals as it is quite difficult to stimulate the mechanism in polycrystals. The high cost of single crystals and low actuation work outputs restrict the potential applications of MSMAs utilizing field-induced variant orientation.

The second mechanism for realizing MFIS in MSMAs is the magnetic field-induced martensitic phase transformation. In this case, the austenite and martensite phase have different magnetic characteristics, expressed in different levels of induced magnetization under external field. At the

6

same time, they are also capable of conventional superelasticity through stress-induced phase transformation. Although these "meta-magnetic SMAs" demonstrate impressive properties, their most important drawback is their extreme brittleness in the polycrystalline state. The most heavily studied meta-magnetic SMAs based on the NiMn system have essentially zero tensile ductility in the solution-treated state. The brittleness in tension was attributed to intergranular failure caused by stress concentration at and weakness of the grain boundaries *(41)* due to the inherent disparity between the bonding strength of atoms across grain boundaries and atoms inside of a grain. Studies have been conducted in order to improve grain boundary toughness by including alloying such as with boron to improve cohesiveness, using grain refinement to limit crack propagation, and introduction of special texture to reduce stress concentration and improve compatibility *(42-44)*. Although some improvement has been observed, the mechanical properties of such materials remain unfit for structural applications.

The recent introduction of a magnetic $Fe_{43.5}Mn_{34}Al_{15}Ni_{7.5}$ SMA (FMAN) *(12-14)* has provided solution to the poor load-bearing capabilities in MSMAs. This material demonstrates a combination of meta-magnetic shape memory effect and robust mechanical properties suitable for structural applications. The co-PI has successfully produced the material in polycrystalline form and demonstrated tensile strength over 800 MPa and ductility exceeding 10% strain, making it one of the first MSMAs capable of simultaneous self-sensing and self-centering when applied in an infrastructure system *(15)*.

FeMnAlNi SMA demonstrates the meta-magnetic shape memory behavior: Figure 3(a) shows the relationship between applied strain on the FeMnAlNi wire and the maximum magnetization. A biasing magnetic field of 500 gauss was applied through a permanent magnetic on the FeMnNiAl wire by adjusting the strength of the magnet and the distance between the magnet and the wire. The magnetic signal was monitored using a thin film magnetometer (Xtrinsic MAG3110) typically found in smartphones. When the composite was pulled in tension and stress-induced phase transformation occurred, the maximum measured magnetization was altered as the martensite phase, which has a different magnetic character from the austenite, is formed. When the material was unloaded, the magnetization returned to the initial values as martensite reverted back to austenite. This means that the change in magnetization can be directly correlated with strain in the wire. The time history comparison of the magnetization changes during the cyclic load-unloading process is shown in Figure 3(b).
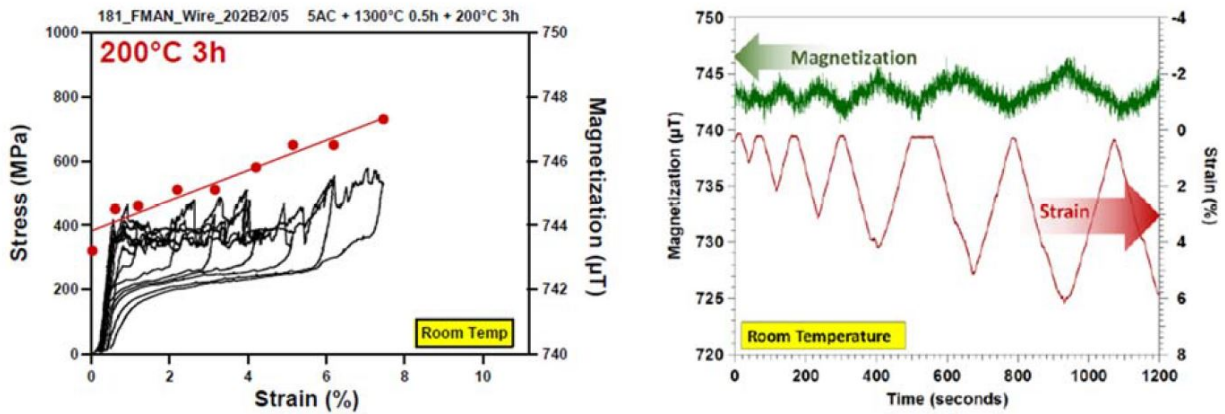
Figure 3. (a) Magneto-mechanical response of FMAN wire with 3 hour precipitation heat treatment: the red dots above stress-strain curve shows the maximum magnetization in the wire measured at a given applied strain level, and (b) time history comparison of magnetization and strain during loading cycles of part a.

The use of magnetic sensing for non-destructive evaluation represents an inherently multidisciplinary research area with respect to both the analysis and experimental domain. The analysis of phase transforming wires embedded in a concrete structure for the generation of a magnetic signal requires a strong understanding of the solid mechanics of the concrete-wire interface, the use of external magnetic sensing (and thus related work with metrology sensitivities, probe placement, and specimen size), and the ability to translate magnetic signals into internal stress fields. Work on monitoring steel corrosion has proven magnetic sensing a viable method of non-destructive evaluation of similar structures, with obtained magnetic signals shown to be significantly strong as compared the background noise present in the system *(45)*. This work also proposes Giant Magneto-Resistive (GMR) sensors, which measure magnetic field strength, as a possible magnetic sensor for non-destructive evaluation of internal steel bars due to low power consumption and a wide sensing range. As for interpreting the detected magnetic fields, computational work has been previously done by Hartl and coworkers to transform signals generated from distributions of distinct embedded SMA domains into internal continuous stress fields *(29)*. The success of the current work requires the development of computational models and experimental work to integrate these previous and current developments into a robust model, with the experimental results correlated to FEA models, leveraging previous FEA and experimental work on SMAs where possible.

4. METHODOLOGY

In this section, three main methodologies to accomplish project objectives are discussed in detail. In order to fabricate large diameter rods of Fe-SMAs, detailed thermomechanical processing steps required to produce polycrystalline alloy is reported. Methods to induce abnormal grain growth to eliminate grain boundary constrains are explained. To characterize mechanical behavior of the wires and cables, new grip designs are demonstrated. Finally, programs used for modelling the theoretical framework for the magnetostatic modelling are explained.

4.1. Description of Materials

Materials used in this work is a Fe-SMA alloy with a nominal composition of Fe-34%Mn-15%Al-7.5%Ni at.%. In the following sections, thermomechanical processing and abnormal grain growth methods are explained in detail to fabricate superelastic Fe-SMA rods.

4.2. Procedures

4.2.1. Fabrication of Large Diameter Rods

One of the main goals of the project is to create large-dimension FMAN rods that are suitable for structural applications. In this study, a rod with 5.5 mm diameter is initially fabricated.

FeMnAlNi bars are first fabricated through vacuum induction melting. 31.7 mm diameter as cast rod is shown in Figure 4.
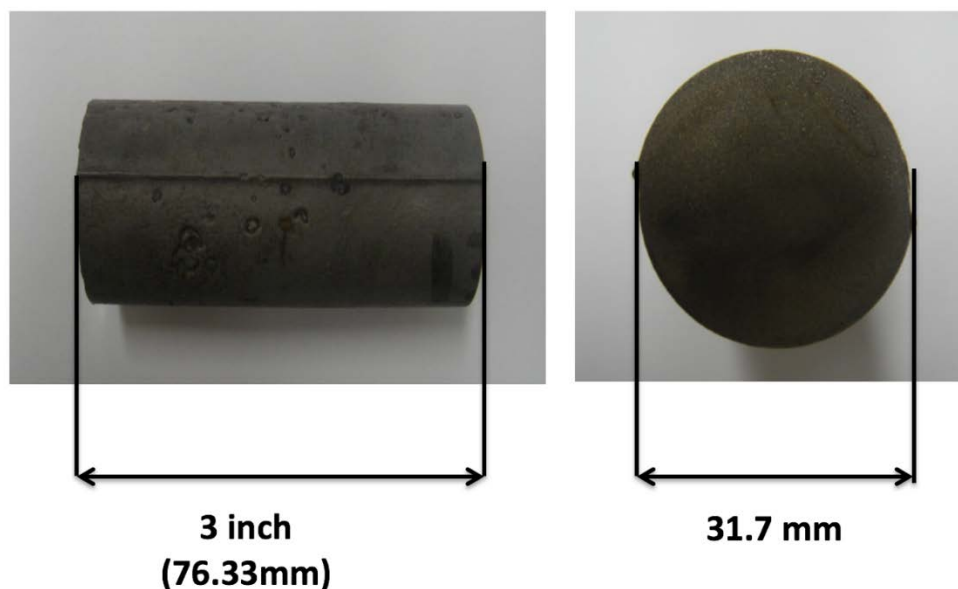
Figure 4. Vacuum induction melted as cast FeMnAlNi alloy.

As cast alloy bar is solution heat treated at 1200°C for 4 hours. Solution heat treated bar is then hot extruded to 5.5 mm rod. Hot extrusion temperature is chosen as 900°C. This temperature creates soft γ second phases in the material that facilitates extrusion process. FeMnAlNi bar after hot extrusion is shown in Figure 5. Cross section view of the rod (Figure 5b) shows 5.5 mm diameter FeMnAlNi bar with a steel can around it.
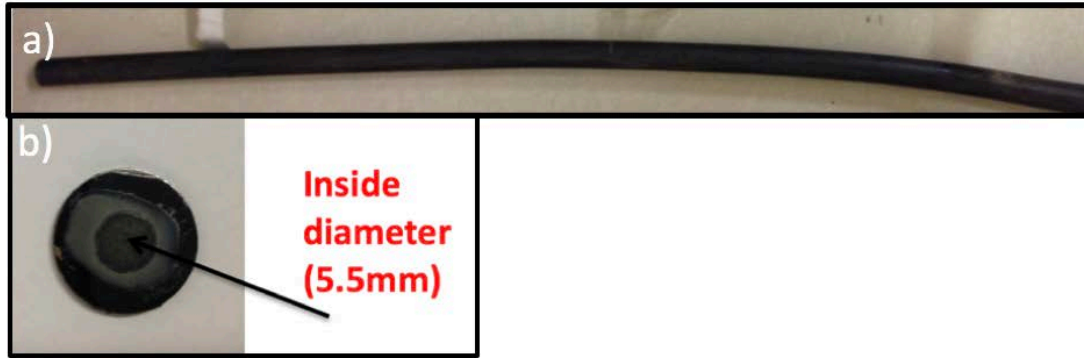
Figure 5. (a) Hot extruded FeMnAlNi bar. (b) Final diameter (5.5 mm) of the extruded bar.

After extrusion, FeMnAlNi bar is cut into 70 mm long specimens and the steel can around the bar is removed by machining. Two different specimens are prepared with a final diameter of 4 and 5 mm for abnormal grain growth experiments.

4.2.2. Abnormal Grain Growth Heat Treatments

Fe-based shape memory alloys usually suffer from large elastic and transformation strain anisotropy. This leads to high internal stresses between grains with large orientation mismatches during martensitic transformation. Additionally, limited number of martensite variants in Fe-based systems inhibits strain accommodation at the grain boundaries and intergranular fracture occurs before the transformation is complete. Therefore, it is necessary to eliminate grain boundary constraints, triple junctions to obtain good super-elasticity. In order to eliminate these constraints, grain size of the material has to be coarse, perpendicular to the rod axis and span the cross section of the wire. The authors have developed a simple technique to obtain large grain size through abnormal grain growth.

A specimen with dimensions of 2 to 4.6 mm in diameter and 70 mm long is encapsulated under inert argon atmosphere using quartz tube. In order to prevent any reaction with the quartz tube, specimens are wrapped with Molybdenum sheet. A series of cyclic heat treatments are performed between 1200°C and room temperature (two phase region) in order to achieve abnormal grains that is required for superelasticity (Figure 6). This heat treatment cycle was repeated for 5 times. Following this, sample is solution heat treated at 1300°C for 30min and quenched in water. Solution heat treatment process ensures to remove second phases that are detrimental for superelasticity.
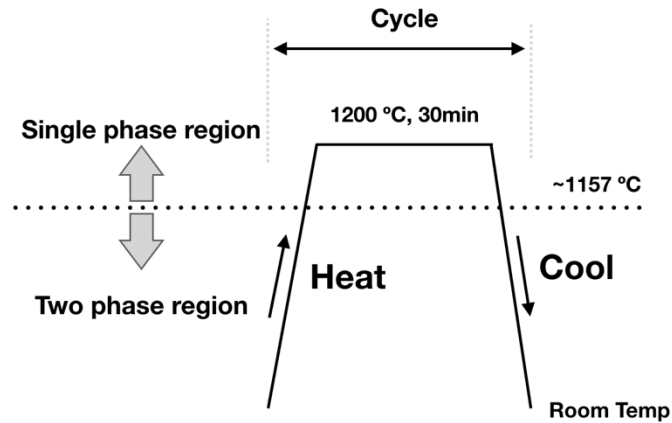
Figure 6. Thermal cycling process for grain growth in Fe-34Mn-15Al-7.5Ni (at. %) alloy. Cycling between single phase and two-phase region promotes grain growth.

After heat treatments, sample is cut using Electric Discharge Machining. One side of the sample is prepared for microstructural investigations and grinded using 400, 800 and 1200 grit paper, respectively. Afterwards, specimen is vibratory polished and prepared for detailed microstructural investigations. The FeMnAlNi bar with 5mm diameter after abnormal grain growth is shown in Figure 7.

Figure 7. FeMnAlNi bar with 4.6 mm diameter subjected to abnormal grain growth heat treatment between 1200°C and room temperature.

4.2.3. Sample Preparation

Sample preparations for microstructural characterization were done as follows:

1. 2 mm diameter Fe-SMA cables were set with epoxy prior to grinding
2. 4.6 mm diameter rods cut into half prior to grinding.
3. All samples were grinded using a SiC paper to 180, 320, 400, 600, 800, 1000 and 1200 grits.
4. After grinding, samples were polished with 6-, 3-, 1-, 0.25- and 0.1-micron diamond suspension.

11

5. Samples were vibratory polished using colloidal silica.
6. After polishing, samples were cleaned using acetone and alcohol.

4.3. Apparatus/Equipment Used

In this section, microstructural cauterization tools that is used to investigate grain size and orientation of the large diameter Fe-SMA rods are explained. In order to test large diameter cables, current tensile testing grips were redesigned to improve the contact force and prevent slipping during testing. In this section, apparatus design methodologies are explained in detail.

4.3.1. Microstructural Characterization

Microstructural investigations are performed using optical microscopy and electron backscatter diffraction (EBSD) technique. Grain size, morphology, phases and crystal orientations were determined through microstructural investigations.

4.3.2. Mechanical Testing

In order to measure the change in magnetic behavior of the large dimension Fe-SMA rods and validate simulation efforts, rod testing grips and an attachment for measuring magnetic changes in the braided cables are developed.

Nonmagnetic Grip Design for Tensile Testing of Large Diameter Fe-SMA Rods: A custom made nonmagnetic grips are needed to examine the superelastic response of large diameter Fe-SMA rods. Collet type grips are advantageous to test large size rods since the collet inner diameter can easily be adjusted to different sizes. Figure 8 shows an example of collets with different inner diameters.

Figure 8. Example collets with different inner diameters.

For testing 2 mm diameter Fe-SMA rods, a custom-made grip with a 2 mm ER-16 type collet type is designed with SolidWorks (Figure 9).
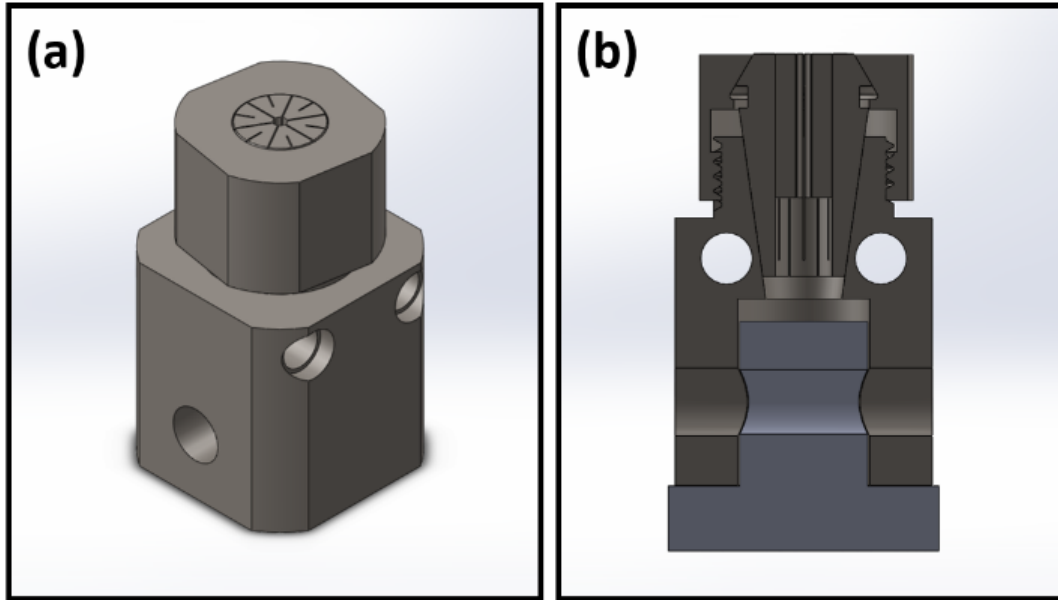
Figure 9. 3D SolidWorks design of the grips with collets.

Custom made grip consist of three parts:

1. <u>Collet</u>: ER-16 type collet with an inner diameter of 2 mm. It is made out of nonmagnetic Inconel alloy.
2. <u>Collet nut:</u> After the sample is inserted inside the collet, this part tightens the collet and helps to provide grip for the sample. It is made out of nonmagnetic Inconel alloy.
3. <u>Base:</u> Base part connects the collet grip into the MTS tension frame rods. It is made out of nonmagnetic Inconel alloy.

Two crucial factors were taken into consideration when the material selection is made; strength and magnetic property. The grip material has to be strong enough to withstand the forces during superelastic testing of large size Fe-SMA rods. The grip materials magnetic permeability has to be close to zero to eliminate magnetic interference. Inconel alloy was chosen as a grip material since it provides both strength and nonmagnetic behavior.

So far collet nut and base part of the grips were fabricated using Inconel alloy. Collet part of the grip is still in production. 3D SolidWorks model of the testing setup and the experimental setup for measuring mechanical and magnetic properties of the large diameter Fe-SMA rods are shown in Figure 10.
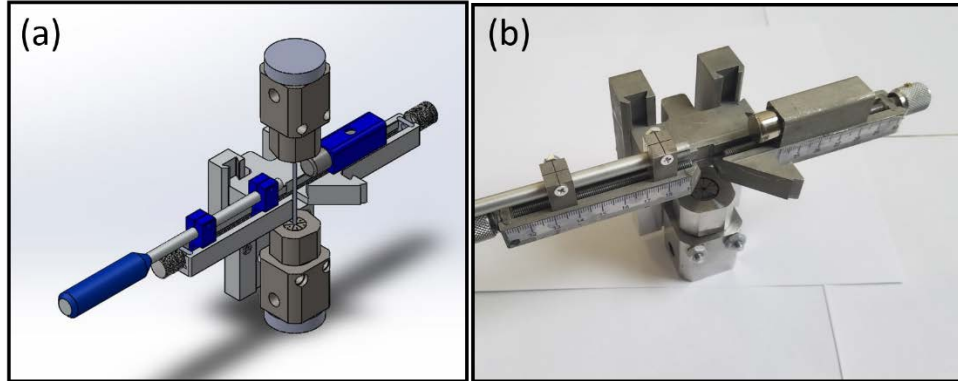
Figure 10. (a) 3D SolidWorks model of the testing setup and (b) experimental setup for measuring magnetic properties of the large diameter Fe-Mn-Al-Ni rods under stress at room temperature.

The attachment contains two rails that can hold the magnetic hall sensor and a biasing magnet at different configurations. The rails allow the sensor and magnet to change their distance horizontally from the wire/cable being tested. The attachment also has the capability to move in the vertical axis. Since the location of the nucleation of the transformation is unknown, vertical movement of the test setup allows scan the rod and characterize location of the martensitic transformation.

In the final setup, a Lakeshore Cryogenics HGT-3010 hall sensor was used. The sensor was delivered along with calibration data provided by Lakeshore. This calibration data was loaded on the hall sensor's cable before being used for testing. The sensor was used in conjunction with a Lakeshore model 460 3 channel gauss meter.

4.4. Software Programs Used

4.4.1. 3D Modelling Design

In this study, 3D Modelling designs are prepared using SolidWorks.

4.4.2. Magneto-Static Modelling

The framework was built in COMSOL Multiphysics (a cross-platform finite element software to solve coupled systems of partial differential equations) to model the magnetic field for a variety of geometries. In the single rod model, the rod is partitioned along the length of the wire into axisymmetric segments, each with a controllable magnetic permeability and size. The local magnetic permeabilities of the rod are inputs using the known magnetic permeability of each martensite volume fraction calculated by the Abaqus structural model.

The rods modeled in COMSOL are constructed using a single rod. In a single, large rod the flux remains fairly constant across the cross-section, For Fe-SMA rods, a change in magnetic permeability would affect the magnetic flux down the rod in addition to near the local phase transformation.

5. ANALYSIS AND FINDINGS

This section discusses the results for the fabrication of large-dimension Fe-SMA rods that are suitable for structural applications and demonstrates the comparable properties to those shown in the wires in first year project. When the dimensions are increased, the total internal length of the grain boundaries should be minimized in the FMAN alloys to minimize the unrecovered strain. The goal of the section 5.1 is to determine maximum component size where a bamboo-like oligocrystalline structure still can be obtained.

5.1. Microstructural Characterization of Large-Diameter Fe-SMA Rods

Large sized Fe-SMA rods were extruded from as cast billets. Abnormal grain growth heat treatments were applied to generate necessary microstructure for superelasticity.

The microstructure of the fabricated large diameter rods was investigated with optical microscopy and electron back scatter diffraction techniques (EBSD).

Microstructure of the 2mm Fe-SMA cable is shown in Figure 11b. Upper map in Figure 11b represents the EBSD crystallographic orientation map of the grains in drawing direction. Bottom map in the Figure 11b represents the EBSD phase map. Blue color and the yellow color in the phase map correspond to austenite and martensite phases respectively.

Orientation map analysis of the austenite matrix in Figure 10 indicates that the 2 mm diameter wire does not have a strong [011] texture which is typical for small diameter (0.5mm) Fe-SMA. The orientation of the grains in 2mm diameter wires in the drawing direction (IPFX) start to vary from the [011] direction and grain orientations close to the [111] direction are observed. They have mixture of [011] and [111] oriented grains as shown as green and blue colors in Figure 10. According to the theoretical calculations on the orientation effect on superelasticity FeMnAlNi alloys with [011] direction are expected to transform 10%. This has also been shown experimentally in our previous work where [011] textured wires transformed 6.7% when aged at 200ºC for 24h. On the other hand [111] oriented grains are expected transform 4%. Therefore superelastic response of the 2mm wires are expected to have a superelastic strain between 10% and 4%.
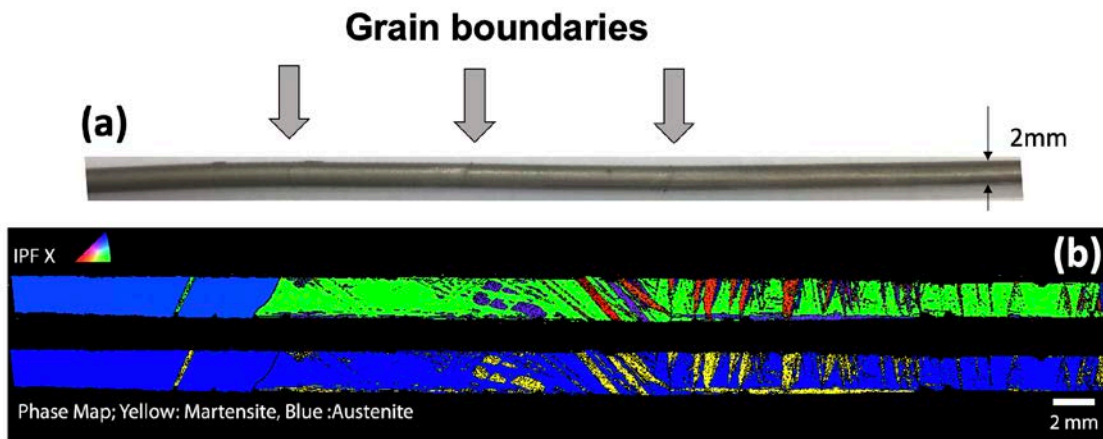
Figure 11. a) Digital image of the 2 mm diameter Fe-Mn-Al-Ni alloy bar with a bamboo structure. b) EBSD orientation mapping of 2 mm Fe-Mn-Al-Ni alloy after AGG. The colors represent the crystal directions parallel to the drawing direction (IPFX) given in the stereographic triangle. Phase map showing the phases present in the microstructure after solution heat treatment. Yellow and blue colors represent martensite and austenite phases respectively.

In FeMnAlNi alloys, the grain size to diameter ratio (d/D) is an important parameter and has to be larger than 1 in order to obtain recoverable superelasticity.

Microstructural analysis showed that 2mm wire consist of large abnormal grains and triple junctions were eliminated. In the grain interiors quench-in martensite phases were observed. Grain boundaries are perpendicular to the wire axis and span across the wire diameter. The d/D ratio for this case is measured around 9.

Figure 12 shows the microstructure of the 4.6 mm rods. Grain boundaries were indicated with a white dotted line in optical microscopy images. Similar to 2 mm diameter rods, abnormal grains were obtained in the 4.6 mm Fe-SMA rods. However, occasionally, small sized grains were found in the microstructure. Grain boundaries are indicated with a white dotted line in optical microscopy images in Figure 11b.
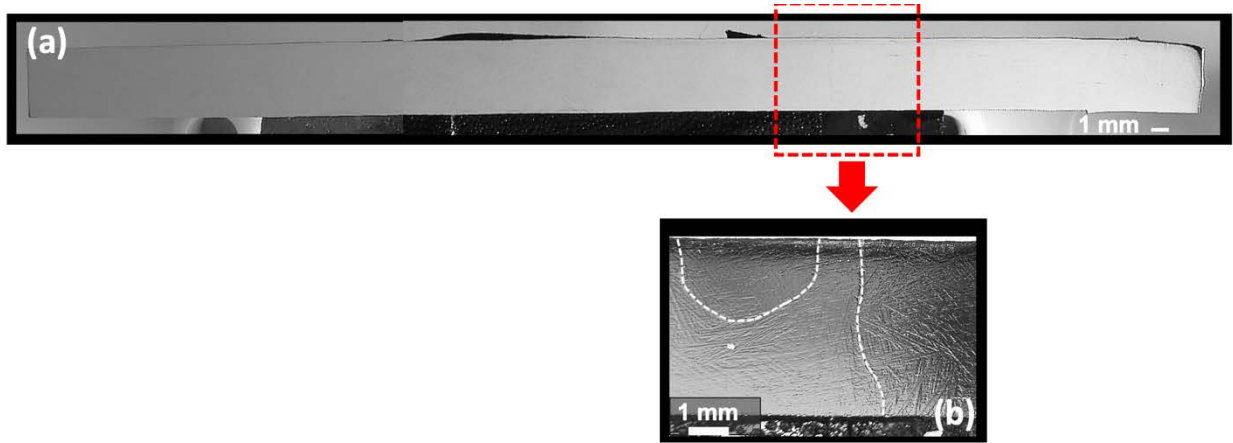
Figure 12. a) OM image of 4.6 mm diameter Fe-Mn-Al-Ni SMA bar. (b) After AGG, grain boundaries span along the wire diameter.

Grain boundaries were perpendicular to the wire axis and span across the wire diameter. On the other hand, small sized grains were found in the microstructure; however, their number density was low. EBSD orientation map shown in Figure 13c represents the crystal directions parallel to extrusion direction (IPFX). It is found that the orientation of the grains in 4.6 mm Fe-SMA rods was different than 2 mm diameter rods and 0.5 mm diameter wires. Unlike small diameter wires, strong texture was not present, and texture was random. This is expected because the wire drawing process usually results in strong fiber texture in alloys.
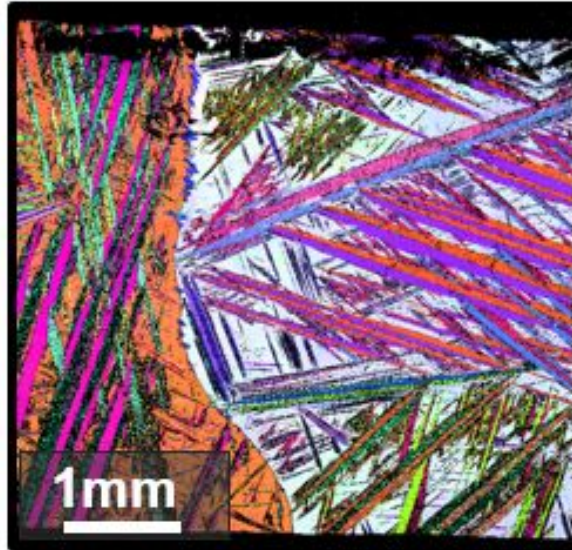
Figure 13. EBSD orientation mapping of the boundary. The colors represent the crystal directions parallel to extrusion direction (IPFX).

Figure 14 shows the EBSD phase map of the 4.6 mm Fe-SMA rod where yellow color represents the martensite, and blue color represents the austenite phase. The results indicate that the microstructure contains a large amount of quench in martensite plates after solution heat treatment. Compositional differences caused by different thermomechanical history between wires and rod can be one possible reason for this increase in quench in martensite volume fraction.

Figure 14. EBSD phase map of the 4.6 mm diameter Fe-SMA rod subjected to abnormal grain growth and solution heat treatment.

5.2. Modelling and Optimization of Magnetic Sensing in Fe-SMAs

This section discusses the results found by using the methods for structural and magnetic evaluation.

More in depth studies on the magnetic sensing and the sensor placement dependencies require a higher resolution model. The updates model, which accounts for different levels of martensitic transformation scripted in MATLAB is shown below in Figure 15.
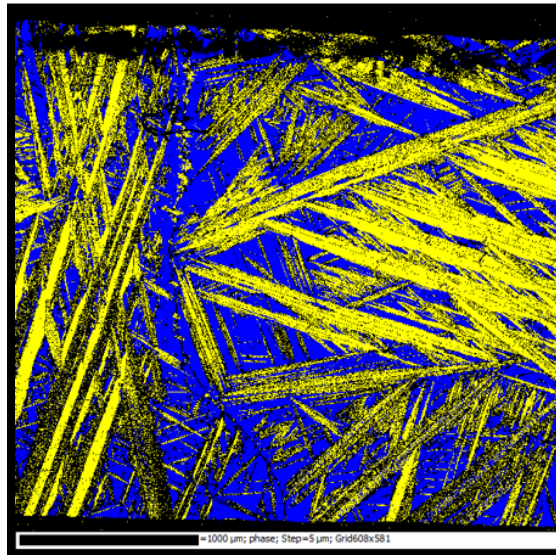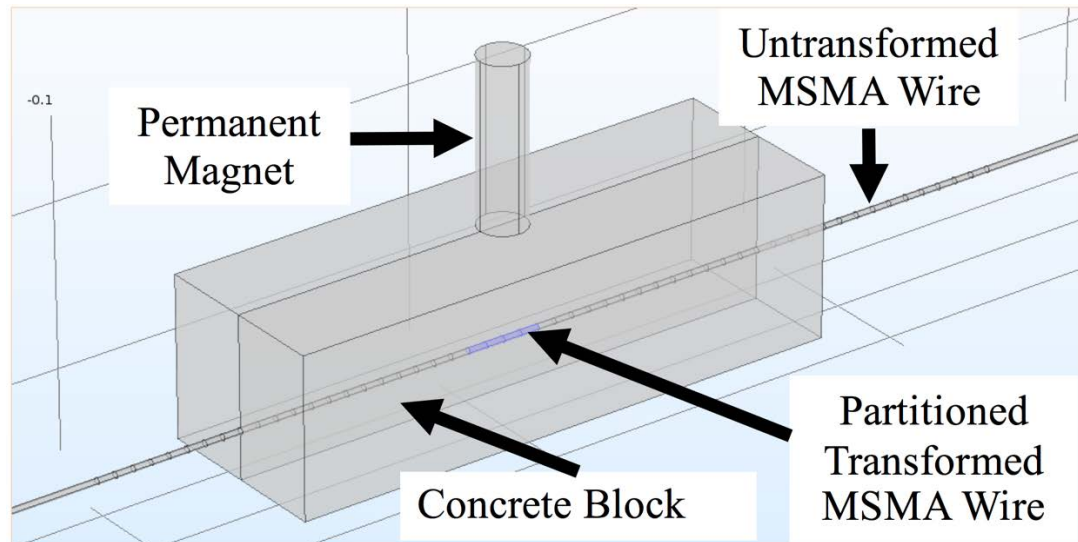

Figure 15. Increased accuracy was gained for the testing the concrete material properties by adding a bottom face sensor. This also allows for standard ASTM strength modulus calculations to be used, since they rely on the bottom deflection to calculate the modulus of rupture in 3 point bend tests.

The material properties are calculated using rule of mixtures based on previous austenite calibration curves shown last month and pulled from the structural model using current material parameters tested as shown in Figure 16. Testing results were improved using a bottom face sensor in addition to the previous testing setup, since the response of the material between the blocks top and bottom faces is no longer estimated and calculated, but directly measured. This allows for better calibration of the concrete material properties to be input into the structural model.
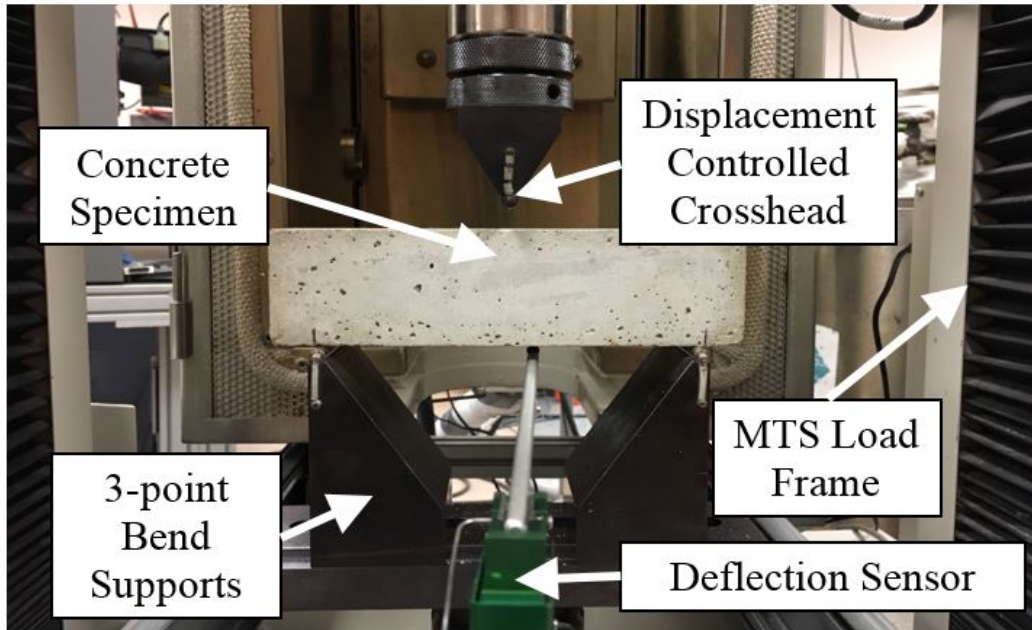
Figure 16. The model now partitions the wire into 5 mm lengths which match the average martensite volume fractions shown in the structural model.

The new structural model results show a clear increase in stress induced martensite near the embedded crack, which extend to clearly delineated regions from 0-10 mm and from 10-15 mm in the structural model. These values led to the magneto-static model using 5 mm partitions to model the material magnetic properties determined in the structural model by the martensite volume fraction. The model and region on increased stress near the crack are shown in Figure 17.
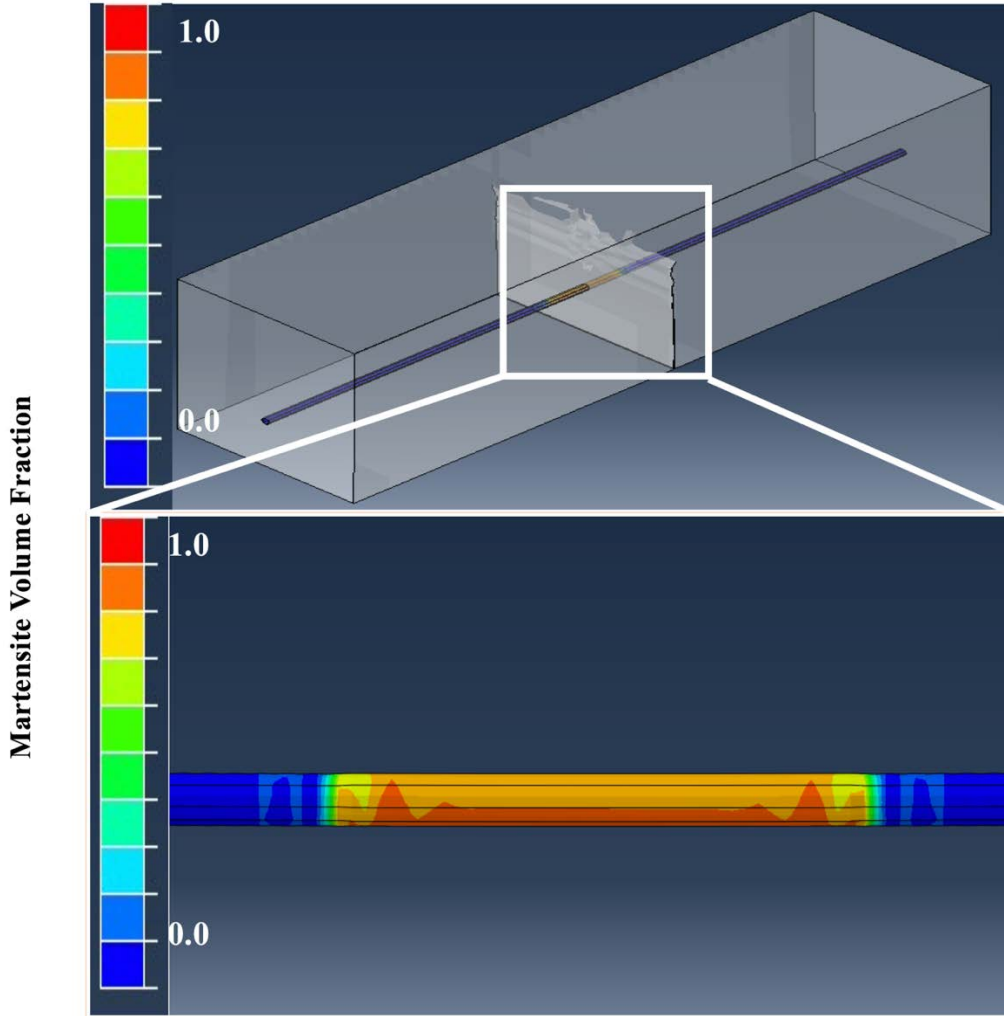
Figure 17. The crack tip stress concentration and subsequent loading and strain transform the SMA wire in the region near the crack.

The resulting martensite volume fractions were then mapped to their respective partitions in the magneto-static model shown first. From the previous studies on same side sensing, it was determined that a sensor-magnet combination set a constant distance from each other moving down the length of the concrete block along the length of the wire was the most effective sensing method found. This encourages a wire closer to the surface, but that will limit the effectiveness of sensing, and may also diminish the change from a structural standpoint if the wire is too close to the surface. From here, a study was performed to determine the relationship between magnetic sensitivity and depth of the wire for a wire with the phase transformation showed above. The study was run for a sensor with a distance of 25 mm away from the magnet center, with the results shown in Figure 18.
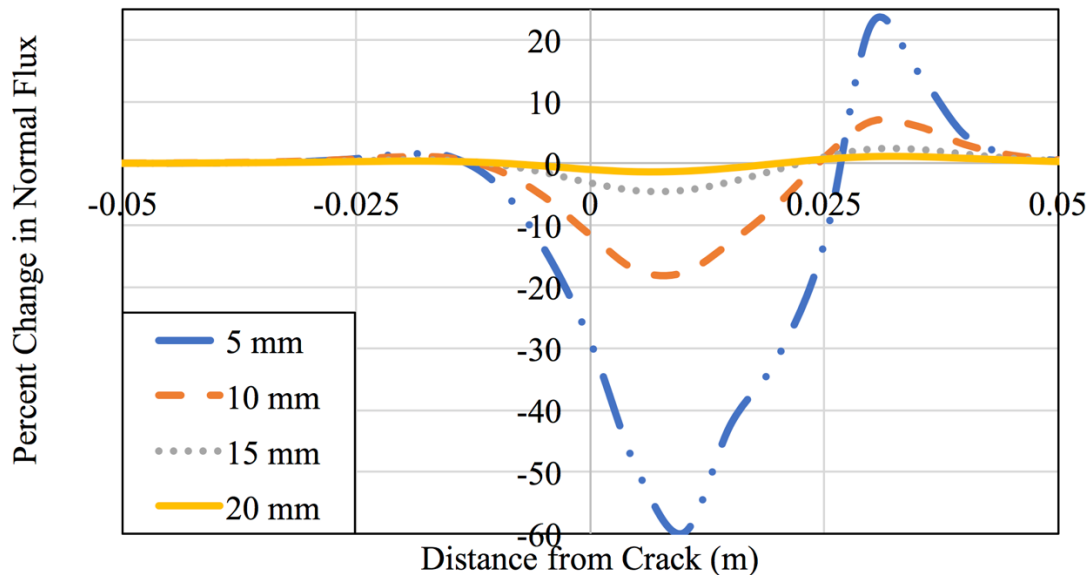
**Figure 18. As the distance the wire was embedded in the structure decreases, the effect the wire has on the magnetic field increases.**

This trade off proves to be very significant, but even the low changes in field strength are still significant with proper noise reduction for this case. The change at 15 mm is approximately 300 µT, which is orders of magnitude larger than published Hall sensor probes with noise reduction circuits while also a larger change than the noise in cheap, standard hall probes available commercially, which is very encouraging.

Work was done on the modeling project to accurately reproduce magnetic testing experimental results near large magnetic gradients to determine the proper geometric design and post-processing for comparing experimental to computational results. Previous computational results were magnetic flux densities at a specified location, but in reality, magnetic probes measure a total flux across a discrete active area, or surface before accounting for the total area to determine the average flux density. The addition of a meshed surface to simulate this active area was developed to mimic the actual hall sensor used in the experimental data, and a study was conducted to investigate the change under SMA transformation near the wire. A model of the transformation of an SMA wire under tensile loading was developed. The wire transforms grain by grain from austenite to martensite, with transformation originating at one of the wire grips, a point of increased stress. The overview of this simulation is shown below in Figure 19.
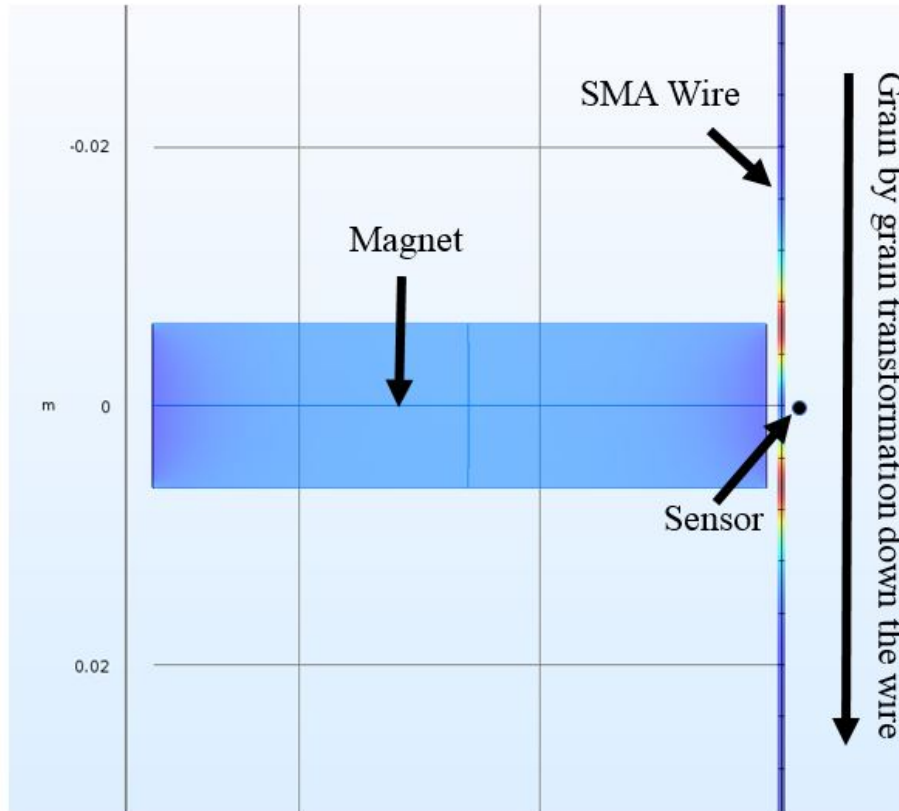
Figure 19. The wire starts fully austenite, with grain by grain transformation occurring down the wire starting from the top of the wire, which is held by wire grips

From here, a discrepancy between the typical far field magnetic trends and the close experimental results presented itself. While results previously shown for far field measurements suggested a transformation from austenite to martensite would lead to an increase in measured normal magnetic field strength, experimental data measured very close to the wire, as shown in Figure 19 showed the opposite trend, with measured normal magnetic flux density decreasing as a result of the austenite to martensite transformation. This is shown in Figure 20, which shares the same black arrow pictured above. Thus, an investigation into the near field trends was performed.

A model of the sensor active area was originally calculated by determining the magnetic flux density at a series of points on the face of the sensor, and geometrically averaged to determine an average magnetic flux density, as opposed to the single point data showed before. While more efficient and consistent, the single point data existed as a physical single solution for a single location, as opposed to an area average over a discrete surface, which requires geometric values for the hall probe. With these values to compare the experimental and computational results, the trends on different parts of the sensor face/active area were plotted to show how the average flux density has different trends near the wire depending on portion of the sensor face. These competing trends lead to the actual, measured response. At different locations on the sensor face, when the wire is very near, the flux density increases along the length of the wire. However, the wire also changes the normal direction of the magnetic flux, which is a stronger response farther away from the wire. The pointwise trends are shown in Figure 21.

22
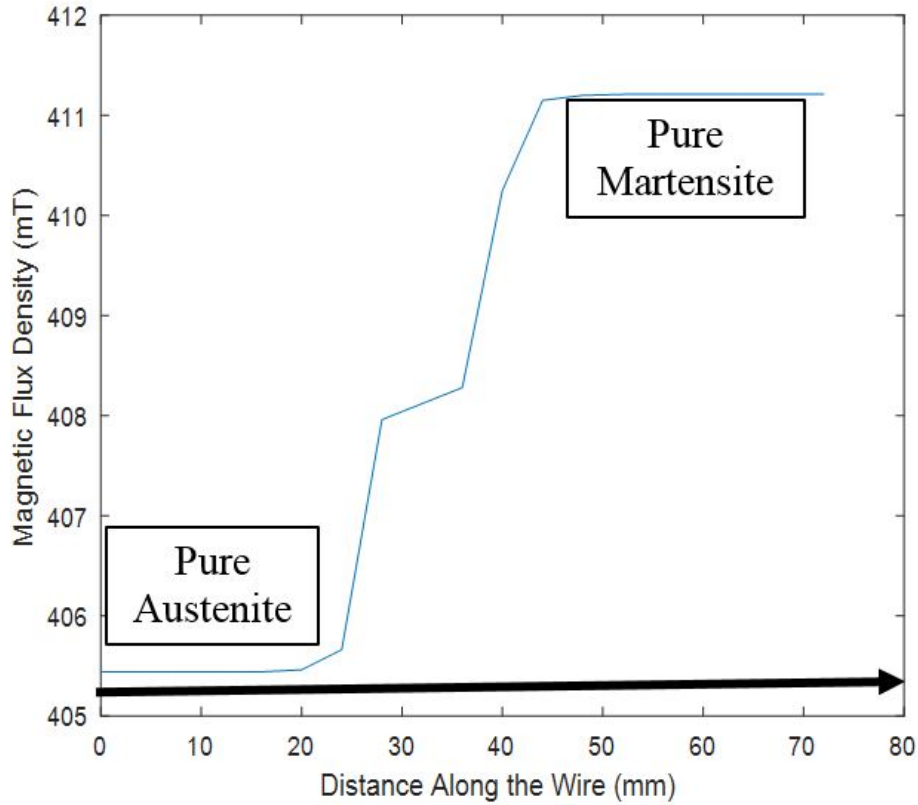
Figure 20. For a 1 mm distance between the wire and sensor, and 1 mm between the wire and magnet face. The wire has a 0.25 mm radius.

The results at these labeled points are shown in Figure 22. The trends from Figure 21 and Figure 22 show a decrease in magnetic flux density along the axis of the wire and an increase in magnetic flux density for points not aligned with the wire. This follows the logic that the magnetizable wire (austenite)
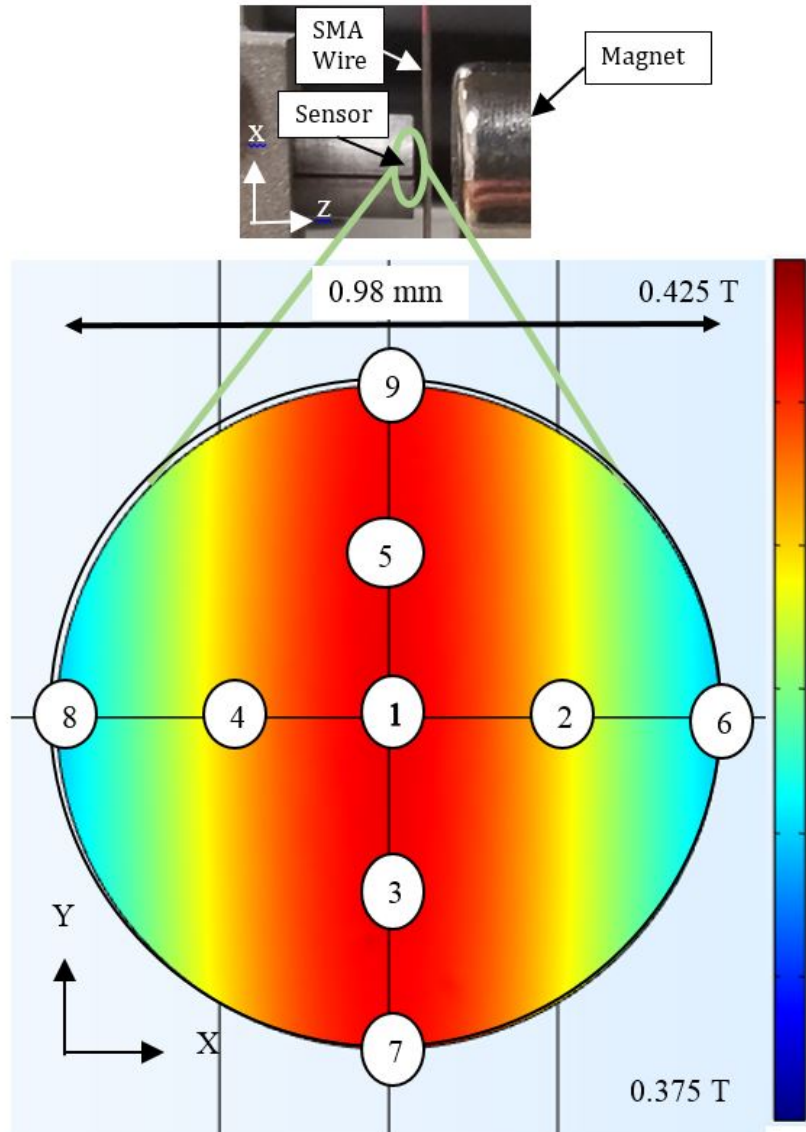
Figure 21. The results of these points under the previous configuration were all measured individually to determine the trends along the magnetic sensor face.

redirects the magnetic field along its length. As such, the field very close to the wire strengthens when the wire is more magnetizable. However, the normal of the magnetic field is also redirected along the length of the wire, which is 90 degrees away from the normal of the sensor face, which decreases the measured magnetic flux density. The first trend only matters very close to the wire, so this trend, which is very strong for this specific configuration, had not been documented until this point. The latter trend, involving the change in the normal direction of the magnetic field, was all that is generally seen at much larger distance between the sensor face and wire.
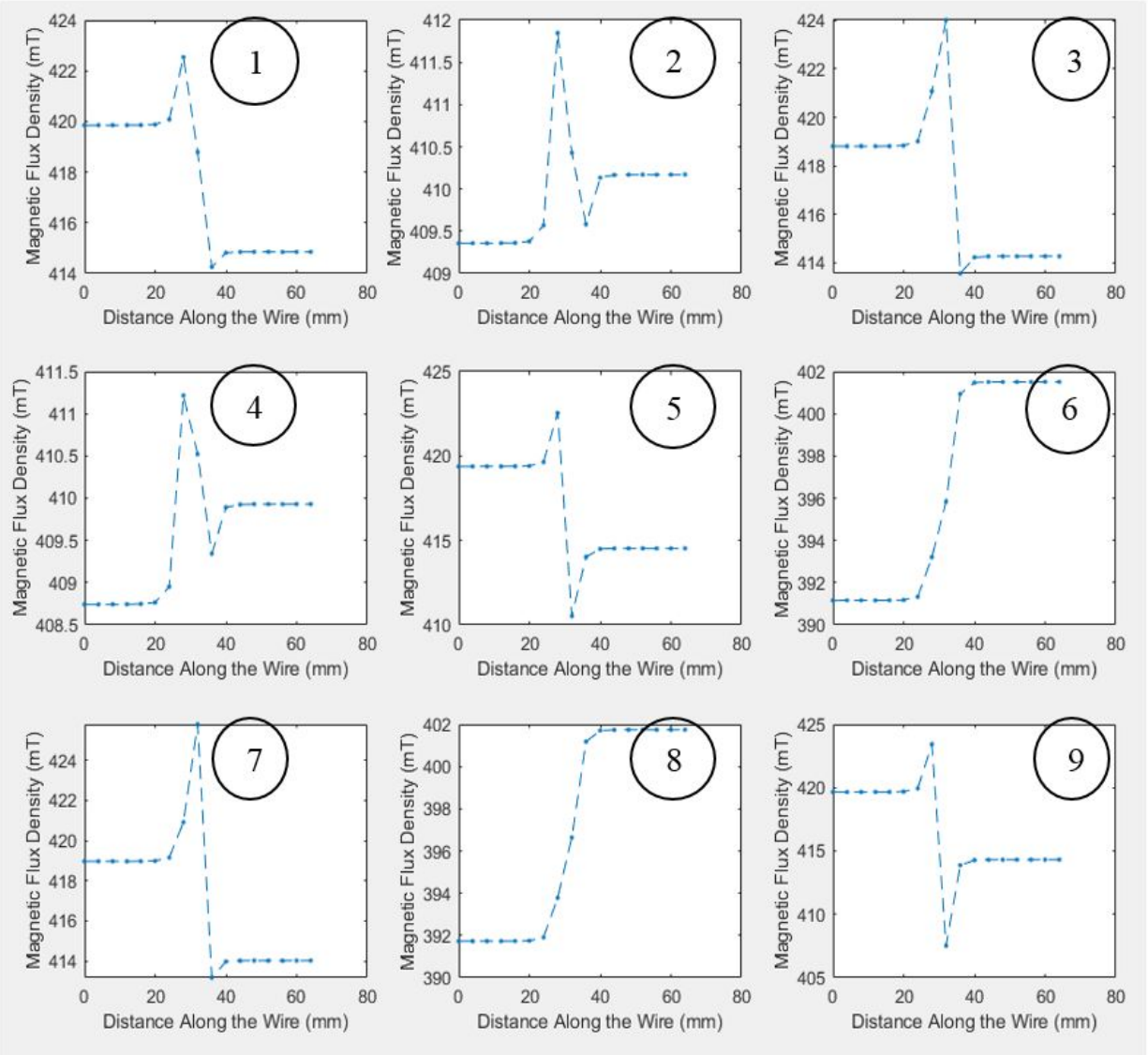
Figure 22. The trends of normal magnetic flux density show an increase in locations aligned with the wire, and a decrease in locations no aligned with the wire.

A visual comparison of Figure 22 would be to compare the magnetic flus density along the sensor face for both austenite and martensite. This is shown in Figure 23, and the same trends can be seen. The magnetic flux density decreases near the wire and along the wire axis but increases as the location moves away from this axis.
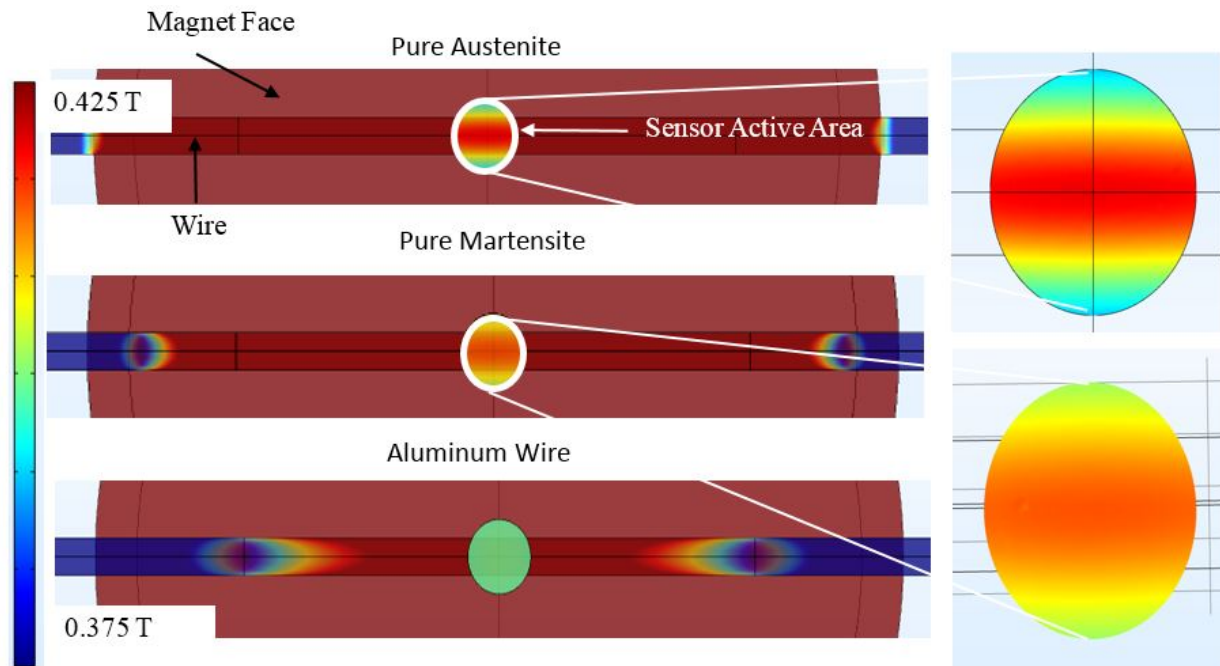
Figure 23. Visual comparison of Figure 21.

Since the effects of the decrease become stronger the closer the sensor is to the wire, placing the sensor close to the wire will yield the experimental decrease seen in testing, while moving the sensor farther away will move the trend back to the previously seen increase due to the change in normal flux when the wire has a higher magnetic susceptibility.

Moving the sensor closer (slightly under 0.5 mm) with a slightly larger distance between the magnet and wire yields the trend of a decrease in average measured normal magnetic flux density as seen experimentally.

Work to correlate computational and experimental work concerning the magnetic sensing of Fe-SMA transformation was conducted using via tensile loading of Fe-SMA wire. A model was developed to simulate a grain by grain transformation of a wire with large (4mm) grains along the wire, modeled as partitioned segments. A magnet was placed on one side of the wire, and a sensor on the other as shown in, and the sensor is modeled as a circular plane in the air domain of the same dimensions as the active area of the experimental work co-linearly on this project.

Other transformation patterns for grain by grain transformation were investigated, and a pattern emerged for sensing very close the wire under transformation. The center of the sensor was subjected to a decrease in magnetic flux density, while the edges of the sensor face saw an increase. The decrease near the center is a local change that was previously unexplored, while the increase is due to the global redirecting of the magnetic field by the magnetizable wire, the effects of which decrease as the wire loses magnetization by transforming from Austenite to Martensite.

The wire transforms from Austenite to Martensite, causing a change in the measured magnetic flux density as shown in Figure 24.
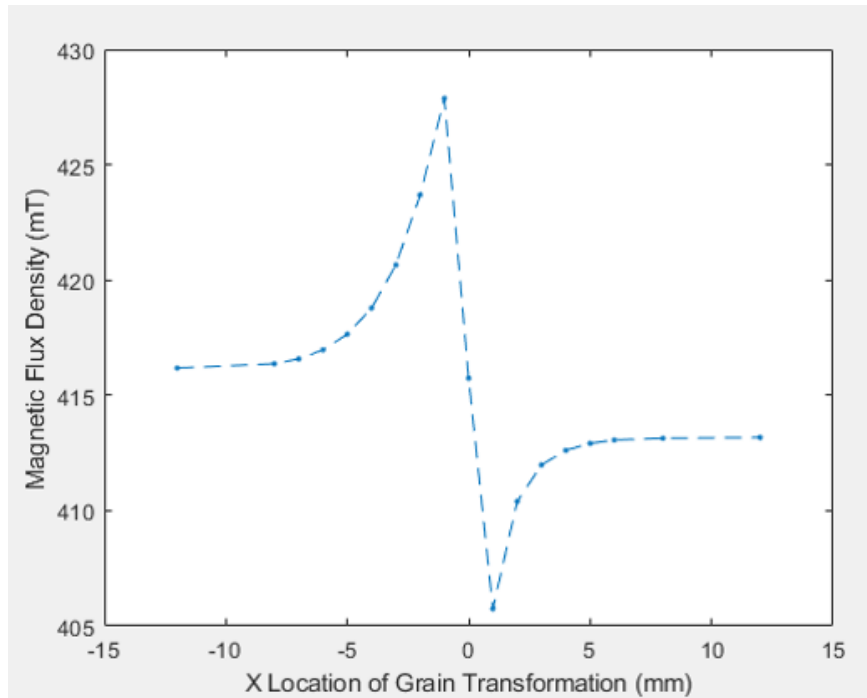
Figure 24. As the wire transforms from Austenite to Martensite (from left to right in the plot, the measured magnetic flux density changes as shown above. There is a large hysteresis due to the redirecting of the magnetic field very close to the sensor.

6. CONCLUSIONS

One of the main objectives of the project is to create large-dimension FMAN rods that are suitable for structural transportation applications. In the current work, fabrication and heat treatment parameters are determined for large Fe-SMAs are solution heat treated at 1200ºC and microstructure of the as cast alloy is prepared for extrusion. Temperature of the hot extrusion is chosen as 900ºC which creates, soft gamma phases in the microstructure. This soft phase facilitates the hot extrusion process. Extrusion process will produce Fe-SMA rods with desired shape. After hot extrusion at 900°C, FeMnAlNi rods are subjected to heat treatments that produces desired microstructure for superelasticity. In order to obtain superelastic response from Fe-SMA rods, it is crucial to have microstructures with coarse, bamboo grains. Therefore, abnormal grain growth methods are performed in the large sized-Fe-SMA rods. After heat treatments large diameter Fe-SMA samples were prepared using mechanical grinding, diamond polishing and vibratory polishing for microstructural investigation. Microstructure of the 2 mm and 4.6 mm diameter rods were characterized using optical microscopy and electron backscatter diffraction pattern images. Abnormal grains were observed in both samples. Grain boundary triple junctions were diminished in the microstructure. Grain size to wire diameter ratio is measured around 9 in large diameter Fe-SMA rods, which is a necessary condition for recoverable superelastic response. These results have shown that the dimeter of the Fe-SMA rods can be increased up to 4.6mm.

A custom made testing setup for measuring mechanical and magnetic response of the large sized Fe-SMA rods was designed using SolidWorks. Collet nut and base part of the setup was fabricated.

The model to evaluate magnetic sensing has increased in efficiency by using suitable partitions based on the structural mechanics results, which have also increased accuracy based on the increased structural testing data. The model has now been used to determine proper sensing configurations and the use of different depth FeMnAlNi rods embedded into structures based on their magnetic disturbances in the field. Recreating magnetic testing results in the simulation framework to determine the observed phenomena involving the magnetic field gradients near a transforming Fe-SMA wire in an induced magnetic field. The model now accounts for the exact hall effect probes used in experimental testing, and characterizes the change along the face of the active area of the sensor, which uses the total magnetic flux density to determine an average, as opposed the a single point at the center. The used of partitioning based on grain by grain transformation has been expanded to control the direction of modeled transformation, and even simulate intra-grain transformation which occurs very quickly, but appears to show up in experimental results, and now can also be modeled in the computational model.

Modelling efforts: Work to correlate computational and experimental work concerning the magnetic sensing of Fe-SMA transformation was conducted using via tensile loading of Fe-SMA wire. A model was developed to simulate a grain by grain transformation of a wire with large (4mm) grains along the wire, modeled as partitioned segments.

This interdisciplinary and collaborative project successfully addresses the challenges associated with the design and materials development of low-cost SMAs and their effective application to civil structures. Findings of this project identifies and develops a pathway for continued commercial development of Fe-SMA rods.

REFERENCES

1. Torra, V., A. Isalgue, F. Martorell, P. Terriault, and F. Lovey. Built in Dampers for Family Homes via SMA: An ANSYS Computation Scheme Based on Mesoscopic and Microscopic Experimental Analyses. *Engineering Structures,* 2007. Volume: 29/1889-1902.

2. Ozbulut, O. E., and S. Hurlebaus. Evaluation of the Performance of a Sliding-Type Base Isolation System with a NiTi Shape Memory Alloy Device Considering Temperature Effects. *Engineering Structures,* 2010. Volume: 32/238-249.

3. DesRoches, R., B. Taftali, and B. R. Ellingwood. Seismic Performance Assessment of Steel Frames with Shape Memory Alloy Connections: Part I—Analysis and Seismic Demands. *Journal of Earthquake Engineering,* 2010. Volume: 14/471-486.

4. Saiidi, M. S., M. O'Brien, and M. Sadrossadat-Zadeh. Cyclic Response of Concrete Bridge Columns Using Superelastic Nitinol and Bendable Concrete. *ACI Structural Journal,* Volume: 2009/106.

5. Saiidi, M. S., and H. Wang. Exploratory Study of Seismic Response of Concrete Columns with Shape Memory Alloys Reinforcement. *ACI Materials Journal,* 2006. Volume: 103/436.

6. Saiidi, M. S., M. Sadrossadat-Zadeh, C. Ayoub, and A. Itani. Pilot Study of Behavior of Concrete Beams Reinforced with Shape Memory Alloys. *Journal of Materials in Civil Engineering,* 2007. Volume 19/454-461.

7. Janke, L., C. Czaderski, M. Motavalli, and J. Ruth. Applications of Shape Memory Alloys in Civil Engineering Structures: Overview, Limits and New Ideas. *Materials and Structures,* 2005. Volume: 38/578-592.

8. Song, G., N. Ma, and H.-N. Li. Applications of Shape Memory Alloys in Civil Structures. *Engineering Structures,* 2006. Volume: 28/1266-1274.

9. Chang, W.-S., and Y. Araki. Use of Shape-Memory Alloys in Construction: A Critical Review. *Proceedings of the Institution of Civil Engineers - Civil Engineering,* 2016. Volume: 169/87-95.

10. Tanaka, Y., Y. Himuro, R. Kainuma, Y. Sutou, T. Omori, and K. Ishida. Ferrous Polycrystalline Shape-Memory Alloy Showing Huge Superelasticity. *Science,* 2010. Volume: 327/1488-1490.

11. Ma, J., and I. Karaman. Expanding the Repertoire of Shape Memory Alloys. *Science,* 2010. Volume: 327/1468-1469.

12. Omori, T., K. Ando, M. Okano, X. Xu, T. Tanaka, I. Ohnuma, R. Kainuma, and K. Ishida. Superelastic Effect in Polycrystalline Ferrous Alloys. *Science,* 2011. Volume: 333/68-71.

13. Tseng, L. W., J. Ma, B. C. Hornbuckle, I. Karaman, G. B. Thompson, Z. P. Luo, and Y. I. Chumlyakov. The Effect of Precipitates on the Superelastic Response of [1 0 0] Oriented FeMnAlNi Single Crystals Under Compression. *Acta Materialia,* 2015. Volume: 97/234-244.

14. Tseng, L. W., J. Ma, S. J. Wang, I. Karaman, M. Kaya, Z. P. Luo, and Y. I. Chumlyakov. Superelastic Response of a Single Crystalline FeMnAlNi Shape Memory Alloy Under Tension and Compression. *Acta Materialia,* 2015. Volume: 89/374-383.

15. Tseng, L. W., J. Ma, M. Vollmer, P. Krooss, T. Niendorf, and I. Karaman. Effect of Grain Size on the Superelastic Response of a FeMnAlNi Polycrystalline Shape Memory Alloy. *Scripta Materialia,* 2016. Volume: 125/68-72.

16. Ozbulut, O. E., S. Hurlebaus, and R. Desroches. Seismic Response Control Using Shape Memory Alloys: A Review. *Journal of Intelligent Material Systems and Structures,* 2011. Volume: 22/1531-1549.

17. Dolce, M., D. Cardone, and R. Marnetto. Implementation and Testing of Passive Control Devices Based on Shape Memory Alloys. *Earthquake Engineering & Structural Dynamics,* 2000. Volume: 29/945-968.

18. Zhu, S., and Y. Zhang. Seismic Behaviour of Self-Centring Braced Frame Buildings with Reusable Hysteretic Damping Brace. *Earthquake Engineering & Structural Dynamics,* 2007. Volume: 36/1329-1346.

19. Silwal, B., O. E. Ozbulut, and R. J. Michael. Seismic Collapse Evaluation of Steel Moment Resisting Frames with Superelastic Viscous Damper. *Journal of Constructional Steel Research,* 2016. Volume: 126/26-36.

20. Walter Yang, C.S., R. DesRoches, and R. T. Leon. Design and Analysis of Braced Frames with Shape Memory Alloy and Energy-Absorbing Hybrid Devices. *Engineering Structures,* 2010. Volume: 32/498-507.

21. McCormick, J., R. DesRoches, D. Fugazza, and F. Auricchio. Seismic Assessment of Concentrically Braced Steel Frames with Shape Memory Alloy Braces. *Journal of Structural Engineering,* 2007. Volume: 133/862-870.

22. Casciati, F., and L. Faravelli. A Passive Control Device with SMA Components: From the Prototype to the Model. *Structural Control and Health Monitoring,* 2009. Volume: 16/751-765.

23. Ozbulut, O. E., and S. Hurlebaus. A Comparative Study on the Seismic Performance of Superelastic-Friction Base Isolators against Near-Field Earthquakes. *Earthquake Spectra,* 2012. Volume: 28/1147-1163.

24. Andrawes, B., and R. DesRoches. Unseating Prevention for Multiple Frame Bridges Using Superelastic Devices. *Smart Materials and Structures,* 2005. Volume: 14/S60-S67.

25. Ma, J., B. Kockar, A. Evirgen, I. Karaman, Z. P. Luo, and Y. I. Chumlyakov. Shape Memory Behavior and Tension–Compression Asymmetry of a FeNiCoAlTa Single-Crystalline Shape Memory Alloy. *Acta Materialia,* 2012. Volume: 60/2186-2195.

26. Ma, J., B. C. Hornbuckle, I. Karaman, G. B. Thompson, Z. P. Luo, and Y. I. Chumlyakov. The Effect of Nanoprecipitates on the Superelastic Properties of FeNiCoAlTa Shape Memory Alloy Single Crystals. *Acta Materialia,* 2013. Volume: 61/3445-3455.

27. Tseng, L. W., J. Ma, I. Karaman, S. J. Wang, and Y. I. Chumlyakov. Superelastic Response of the FeNiCoAlTi Single Crystals Under Tension and Compression. *Scripta Materialia,* 2015. Volume: 101/1-4.

28. Ozcan, H., J. Ma, S. J. Wang, I. Karaman, Y. Chumlyakov, J. Brown, and R. D. Noebe. Effects of Cyclic Heat Treatment and Aging on Superelasticity in Oligocrystalline Fe-Mn-Al-Ni Shape Memory Alloy Wires. *Scripta Materialia,* 2017. Volume: 134/66-70.

29. Goulbourne, N. C., B. R. Bielefeldt, A. A. Benzerga, and D. J. Hartl. Analysis of Shape Memory Alloy Sensory Particles for Damage Detection via Substructure and Continuum Damage Modeling. 2016. Volume: 9800/98000B.

30. Liu J., N. Scheerbaum, J. Lyubina, O. Gutfleisch. Reversibility of Magnetostructural Transition and Associated Magnetocaloric Effect in Ni-Mn-In-Co Applied Physics Letters. 2008. Volume: 93/102512.

31. Murray S.J., M. A. Marioni, A.M. Kukla, J. Robinson, R.C. O'Handley, S.M. Allen. Large field-induced strain in single crystalline Ni–Mn–Ga ferromagnetic shape memory alloy, Journal of Applied Physics. 2000. Volume: 87/5774–5776.

32. Sozinov A, A.A. Likhachev, N. Lanska, K. Ullakko. Giant magnetic-field-induced strain in NiMnGa seven-layered martensitic phase, Applied Physics Letters. 2002. Volume: 80/1746–1748.

33. Marioni M.A., R.C. O'Handley, S.M. Allen, S.R. Hall, D.I. Paul, M.L. Richard, J. Feuchtwanger, B.W. Peterson, J.M. Chambers, R. Techapiesancharoenkij. The ferromagnetic shape-memory effect in Ni–Mn–Ga. Journal of magnetism and magnetic materials. 2005. Volume: 290/35-41.

34. Karaca H.E., I. Karaman, B. Basaran, Y.I. Chumlyakov, H.J. Maier. Magnetic Field and Stress Induced Martensite Reorientation in NiMnGa Ferromagnetic Shape Memory Alloy Single Crystals, Acta Materialia. 2006. Volume: 54/233-245.

35. Karaman I, B. Basaran, H.E. Karaca, A.I. Karsilayan, Y.I. Chumlyakov. Energy harvesting using martensite variant reorientation mechanism in a NiMnGa magnetic shape memory alloy. Applied physics letters. 2007. Volume: 90/172505.

36. Suorsa, I., E. Pagounis and K. Ullakko. Magnetic shape memory actuator performance. Journal of magnetism and magnetic materials. 2004. Volume: 272-276/2029-2030.

37. Heczko, O., A. Sozinov and K. Ullakko Giant field-induced reversible strain in magnetic shape memory NiMnGa alloy, IEEE Transactions on Magnetics. 2000. Volume: 36/3266-3268.

38. James R.D., R. Tickle, M. Wuttig. Large field-induced strains in ferromagnetic shape memory materials, Materials Science and Engineering A. 1999. Volume: 273-275/320-325.

39. Sasso C.P., M. Pasquale, G. Bertotti, V.A. L'vov, V.A. Chernenko. Temperature dependence of mechanical and magnetic curves in Ni2MnGa single crystals, IEEE Transactions on Magnetics. 2003. Volume: 39/3399-3401.

40. Heczko, O., L. Straka. Temperature dependence and temperature limits of magnetic shape memory effect, Journal of Applied Physics. 2003. Volume: 94/7139-7143.

41. Li Y., Y. Xin, C. Jiang, H. Xu. Shape memory effect of grain refined Ni54Mn25Ga21 alloy with high transformation temperature, Scripta Materialia. 2004. Volume: 51/849

42. Liu C, W. Cai, X. An, L. Gao, Z. Gao, L. Zhao. Preparation and characterization of NiMnGa high temperature shape memory alloy thin films using rf magnetron sputtering method, Materials Science and Engineering A. 2006. Volume: 986/438 ‐ 440.

43. Inoue A, H. Tomioka, T. Matsumoto. Microstructure and mechanical ‐ properties of rapidly quenched L12 in Ni-Al-X systems, Metallurgical Transactions A. 1983. Volume: 14/1367.

44. Russell A.M. Ductility in intermetallic compounds, Advanced Engineering Materials. 2003. Volume: 5/629.

45. Tomizuka, M., J. S. Popovics, C.-B. Yun, G. E. Gallo, M. Shelton, V. Giurgiutiu, and P. L. Chapman. A Magnetic Sensing Approach to Characterize Corrosion in Reinforced Concrete. 2007. Volume: 6529/65291A.